Materials and Design 183 (2019) 108133

Contents lists available at ScienceDirect

Materials and Design

journal homepage: www.elsevier.com/locate/matdes

3D printing of polymer-bonded magnets from highly concentrated, plate-like particle suspensions

Alan Shen [a], Xiaoguang Peng [a], Callum P. Bailey [b], Sameh Dardona [b], Anson W.K. Ma [a,c,*]

[a] Department of Chemical and Biomolecular Engineering, University of Connecticut, Storrs, CT 06269, USA
[b] United Technologies Research Center, East Hartford, CT 06118, USA
[c] Polymer Program, Institute of Materials Science, University of Connecticut, Storrs, CT 06269, USA.

HIGHLIGHTS

- 3D printing of polymer-bonded magnets using plate-like, melt-spun magnetic particles yields stronger magnets.
- Mixing two different sizes of particles lowers the overall viscosity, taking advantage of the rheological Farris effect.
- Controlling the rheology enables 3D printing of polymer-bonded magnets with the best magnetic performance reported thus far.

GRAPHICAL ABSTRACT

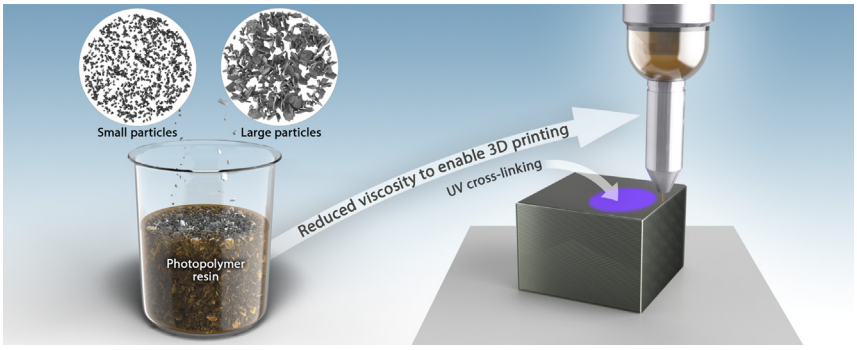

ARTICLE INFO

Article history:
Received 23 April 2019
Received in revised form 16 August 2019
Accepted 17 August 2019
Available online 21 August 2019

Keywords:
3D printing
Magnets
Rheology
Direct write
Suspensions

Data availability:
The raw/processed data required to reproduce these findings cannot be shared at this time due to technical or time limitations.

ABSTRACT

This paper reports the 3D printing of polymer-bonded magnets using highly concentrated suspensions of non-spherical magnetic particles. In a previous study, magnets of arbitrary shapes have been successfully fabricated using the UV-Assisted Direct Write (UADW) method. The magnetic remanence (B_r) of the UADW magnets was limited by the type of magnetic particles used and the highest printable particle loading. Magnetic particles produced from melt spinning have better intrinsic magnetic properties, but their plate-like shape has resulted in a higher working viscosity, posing a major challenge in 3D printing with UADW. Inspired by the "Farris effect" in rheology, we mixed the plate-like particles of two different sizes to increase the polydispersity and reduce the overall viscosity of the mixture as the smaller particles can now fill the interstitial space between the larger ones. Using this rheological technique, a particle loading of as high as 65% by volume, or 93% by weight, was 3D printed. The resulting magnet has a density of 5.2 g/cm^3, an intrinsic coercivity (H_{ci}) of 9.39 kOe, a remanence (B_r) of 5.88 kG, and an energy product ($(BH)_{max}$) of 7.26 MGOe, marking the highest values reported for 3D printed polymer-bonded magnets.

1. Introduction

For magnet fabrication, 3D printing offers design freedom in terms of geometry, composition [1], and particle orientation [2] compared with

* Corresponding author at: University of Connecticut, Storrs, CT 06269, USA.
E-mail address: anson.ma@uconn.edu (A.W.K. Ma).

https://doi.org/10.1016/j.matdes.2019.108133

conventional sintering [3] and injection molding [4] methods. Recently, 3D printing of polymer-bonded magnets has gained research interest over traditional magnet fabrication techniques because of advantages such as reduced material waste and minimal tooling [6–14]. Big Area Additive Manufacturing (BAAM) [5], Fused Deposition Modeling [6], Selective Laser Sintering (SLS) [7,8], Binder jetting [9], Thermo-curing Direct Write [10], and more recently UV-Assisted Direct Write (UADW) method [1] have been demonstrated for magnet fabrication. Among all the reported methods, magnets fabricated using the UADW method stand out both in terms of surface finish (smoothness) and magnetic performance. In this method, ferromagnetic particles (NdFeB) are first dispersed in a UV curable polymer binder, forming a paste at high particle loadings. This paste is then extruded through a nozzle tip and subsequently cured by a UV light source layer-by-layer to fabricate magnets of arbitrary shapes. Further, UADW may be combined with surface mapping and a rotary stage to print functional components (e.g., sensors) directly and conformally onto actual machine parts, allowing seamless integration of functionality into parts with different form factors.

For polymer-bonded magnets, it is well established that increasing the ratio of magnetic powder to non-magnetic binder will increase the remanence and energy product, thereby improving the magnetic performance [11]. However, increasing the powder loading also makes mixing more difficult and increases the chance of particle jamming and nozzle clogging. Further, the ink viscosity may also become too high to be printed, as limited by the printing pressure and flow instabilities [12]. Physically, the increase of viscosity is caused by an increase in both the hydrodynamic interactions and particle-particle interactions as the particle loading increases. At exceedingly high particle loadings, particle-particle interactions become increasingly important [13,14].

In our previous work [5], spherical magnetic particles prepared by an atomization process were used. However, the cooling rate of the atomization process is about two orders of magnitude lower than that of melt spinning [15]. The lower cooling rate results in weaker magnetic phases and the inclusion of non-magnetic elements, limiting the magnetic properties of the powder. Particles prepared from melt spinning is preferred because of the better intrinsic magnetic properties. However, melt spun particles tend to have a non-spherical shape, which has important implications on the rheology and printability. Unlike spherical particles, non-spherical particles tend to rotate or tumble in shear flow, increasing particle-particle interactions and resulting in a higher overall viscosity [16,17]. This is especially true if the particles are not aligned along the shear plane. Highly concentrated suspensions containing non-spherical particles poses a processing challenge because these suspensions generally have a higher working viscosity compared to spherical particle suspensions (for the same particle volume fraction) [16]. This greatly limits the highest printable particle loading and consequently the printed magnet performance.

This paper aims to address the aforementioned processing challenge associated with printing highly concentrated non-spherical particles. The end goal of maximizing the performance of the printed magnets is achieved by understanding the role of particle size and shape on the suspension rheology. More specifically, the effects of average particle size and particle size distribution on rheology have been characterized. The resultant magnets showed the best performance, in terms of relative remanence, relative coercivity, and energy product, compared to all previously reported 3D printed magnets.

2. Experimental methods

2.1. UV-Assisted Direct Write (UADW)

The UADW process employs pneumatically-driven nScrypt tabletop series micro-dispensing equipment. To enable the printing of suspensions having a high particle concentration and a high viscosity, the maximum feed pressure of the system was upgraded from 50 psi to 100 psi. The penetration depth of UV depends on the wavelength and the loading of the particles, and a UV wavelength of 405 nm was chosen based on our previous work [1]. A lens with a focal length of ca. 10 mm was used to focus the UV onto a freshly printed layer. As a rule of thumb, the nozzle size should be at least ten times larger than the characteristic size of the particles [18]. In this study, unless otherwise specified, a layer thickness of 800 μm and a dispensing tip with a 1.6-mm inner diameter was used to minimize clogging and to reduce the pressure drop through the tip.

As illustrated in Fig. 1, the system deposited the first layer onto a transparent polyimide substrate with a printing speed of 5 mm/s. Next, the UV light source irradiated the printed pattern at a moving speed of 2 mm/s following the same tool path [19,20]. The distance between the UV lens and the freshly printed layer was kept at the optimal focal length of 10 mm. The UV cured the layer before the next layer was printed on top. The process was repeated until the entire structure was completed. After that, the complete printed structure was inverted and UV was irradiated through the underside of the polyimide substrate to further cure the bottom of the printed part. The printed structure was then removed from the substrate, giving a freestanding "green" product. The product was further post-cured under a high-density multiple wavelength UV lamp (UVP B-100A), followed by heat treatment at 60 °C (Binder FED 115 oven) for 1 h. Post-curing was applied to increase the degree of cure and improve the mechanical properties. The weight and volume of the samples were then measured to calculate the density of the printed products. For comparison, a "casted" sample was prepared by thermally curing 65 vol% ink at 120 °C for 1 h and the cured sample was machined into a cube. The sample was then magnetized and benchmarked against printed magnets.

2.2. Material

The powder used in this study is MQP-B-20076 isotropic non-spherical NdFeB powder. The as-received particles were produced by melt spinning, having four average particle sizes of 5, 20, 80, and 200 μm and a specific gravity of 7.6 g/cm^3. According to the manufacturer, the intrinsic coercivity (H_{ci}), remanence (B_r), and energy product ($(BH)_{max}$) are 9.1–9.8 kOe, 8.78–8.98 kG, and 14.7–15.7 MGOe, respectively. Around 5% performance degradation is expected for finer 5 and 20 μm particles size due to oxidation. The 20-, 80- and 200-μm particles were further sieved to reduce the size distribution. A particle size analyzer equipped with tri-laser technology (Microtrac S3500 series) was used to determine the particle size distribution of the sieved powder. Dry measurements were carried out in triplicate using air as the medium to convey the sample to the measuring cell. Bimodal samples were then prepared by mixing any two of the sieved samples at different ratios before the UV binder was added.

Formlabs® clear photopolymer resin binder was chosen as the fluid carrier for the NdFeB powder as it yields high NdFeB loading while maintaining sufficiently low viscosity for printing. The resin is composed of methacrylate oligomers and monomers and has a specific gravity of 1.1 g/cm^3. According to Zguris [21], a UV curving wavelength of 405 nm would yield the best mechanical strength for the neat binder. For compounding the powder with the UV binder, a Resodyn LabRAM II acoustic mixer was used at a mixing intensity 100 times gravitation for 5 min to allow thorough and uniform mixing.

2.3. Rheology characterization

Flow curves were measured using a drag-flow rheometer (Physica MCR 702, Anton Paar). Two different fixtures, namely a concentric cylinder and sandblasted parallel plates, were used. Samples with a concentration < 45 vol% were prone to sedimentation, so a concentric cylinder was used [22]. Sandblasted 25-mm parallel plates were used for higher concentration samples (> 45 vol%) to minimize wall slip during tests. The test gap was chosen to be at least ten times than the average particle size to reduce wall effects. The apparent viscosity of the

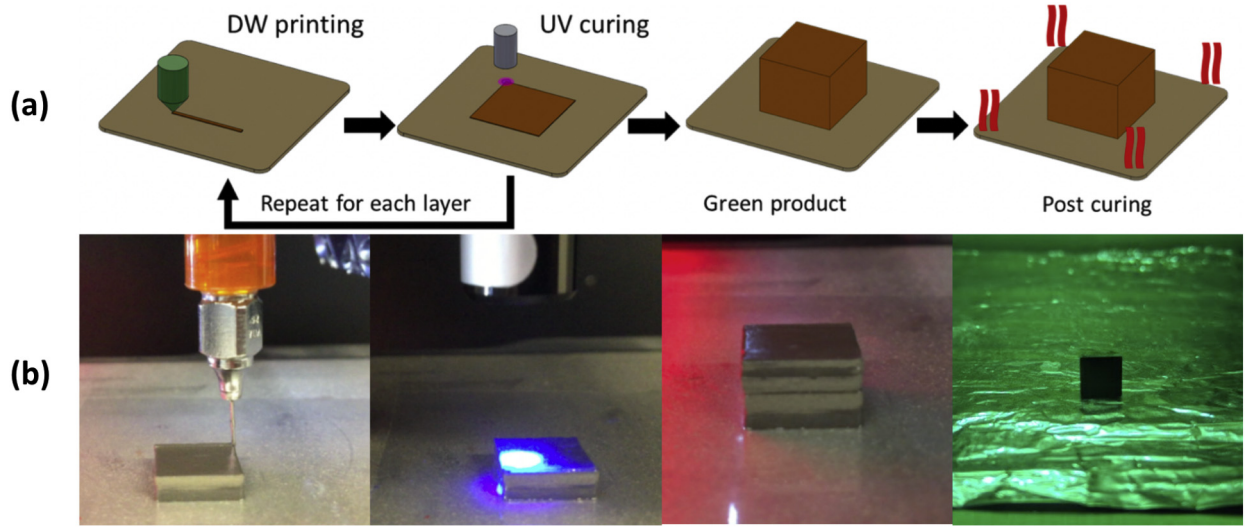

Fig. 1. (a) Schematic diagram and (b) actual images of the UV-assisted direct write (UADW) process for printing a cubic-shaped magnet. The schematic is reproduced from the authors' previous publication [1]. Reprinted with permission from Elsevier.

samples was measured from a shear rate of 0.01 to 25 s^{-1} at 25 °C. In small amplitude oscillatory measurements, parallel plate fixture, a strain amplitude (γ_0) of 1% and a frequency (ω) of 1 rad/s were used.

2.4. Magnetic properties measurements

First, the sample dimensions were measured and recorded. All samples were fully magnetized with a pulsed field of ca. 100 kOe and then second quadrant demagnetization curves were measured on each test sample. The sample under test was placed in the calibrated search coil assembly, then into the gap of an electromagnet. A direct current (DC) magnetizing field of approximately 10 kOe was applied to the magnet in the first quadrant. After applying a forward +10 kOe, the second quadrant B vs. H and (B—H) vs. H demagnetization curve was measured out to the intrinsic coercive field, H_{ci}, at room temperature. All testing was performed using a KJS Associates, Inc. Model HG-700 Computer Automated Magnetic Hysteresigraph System. Testing complies with ASTM A977/A977M-01, "Standard Test Method for Magnetic Properties of High Coercivity Permanent Magnet Materials Using Hysteresigraphs." The B and H-channel is calibrated against a Magnetic Instrumentation Model 2100 Digital Hall-effect Gaussmeter with 0.3% linearity Hall probe and NIST traceable calibration. Overall system accuracy is approximately ±1% for B and ± 2% for H. Data shown in Fig. 6 were collected using a closed-circuit measurement system so no demagnetizing factor correction was applied.

3. Results and discussions

3.1. Particle size and shape characterization

The NdFeB powders used in this study have an average size, or the equivalent spherical diameter, ranging from 5 to 200 μm. The equivalent spherical particle diameter was characterized using a Microtrac S3500 series particle size analyzer based on laser diffraction technology with three lasers. The particle size distribution was calculated from the scattered light signals using a proprietary method and software developed by Microtrac. As shown in Fig. 2, the shape of 5-μm and 20-μm samples are irregular, whereas triangular plate-like particles are clearly visible in the 80-μm and 200-μm samples. Further, if we define the aspect ratio as the longest axis of the particles divided by the shortest axis, the 200-μm sample has a higher aspect ratio than the 80-μm sample, followed by the 20-μm and the 5-μm samples. For high aspect ratio particles, the particle orientation affects the overall viscosity of the system [23]. Theoretically, particles with high aspect ratio will become progressively align along the shear plane as the shear rate increases, leading to a reduction in viscosity and shear thinning [16,24,25]. Fig. 2e shows the detailed distributions of the particle size of all the samples studied. Although the samples have been sieved before use, a size distribution still exists in the unimodal samples.

3.2. Effects of particle concentration and size on ink rheology

Fig. 3a shows the steady shear rheology data of the 20-μm samples at different particle loadings from 0.01 s^{-1} to 25 s^{-1}. Within the shear rate range studied, the neat binder behaved essentially as a Newtonian fluid with a constant shear viscosity of ca. 0.9 Pa.s. Inclusion of NdFeB powder increased the suspension viscosity, especially at low shear rates, leading to shear thinning behavior (i.e., viscosity decreases as a function of increasing shear rate). The degree of shear thinning increases as the powder loading increases. Some degree of shear thinning is considered to be desirable for extrusion-based 3D printing because the shear rate generated the printing process will reduce the ink viscosity for ease of extrusion. As soon as the ink is deposited onto a substrate, the shear rate diminishes, and the corresponding increase in ink viscosity minimizes further fluid spreading, thereby improving shape fidelity of the printed structure. It is worth noting that the viscosities of non-spherical NdFeB suspensions are generally higher than the viscosities of spherical NdFeB suspensions reported previously [1]. This may be explained by the increase of particle-particle interactions due to the irregular shape of the particles as they tumble and make contacts in shear flow.

Different empirical and semi-empirical models exist in the literature to describe the evolution of suspension viscosity as a function of particle volume fraction. Relative viscosity is defined as the suspension viscosity divided by the suspending medium viscosity, or the viscosity of the neat binder in this case. As majority of the existing models were invented and validated for spherical particle suspensions in dilute or semi-dilute regime, there are fewer models available for highly concentrated non-spherical particle suspensions. In this paper, we will limit to two commonly used models proposed by Mooney and Krieger and Dougherty.

Mooney [26] proposed the following equation:

$$\eta_r = \exp\left(\frac{k\phi}{1-\frac{\phi}{\phi_m}}\right),$$

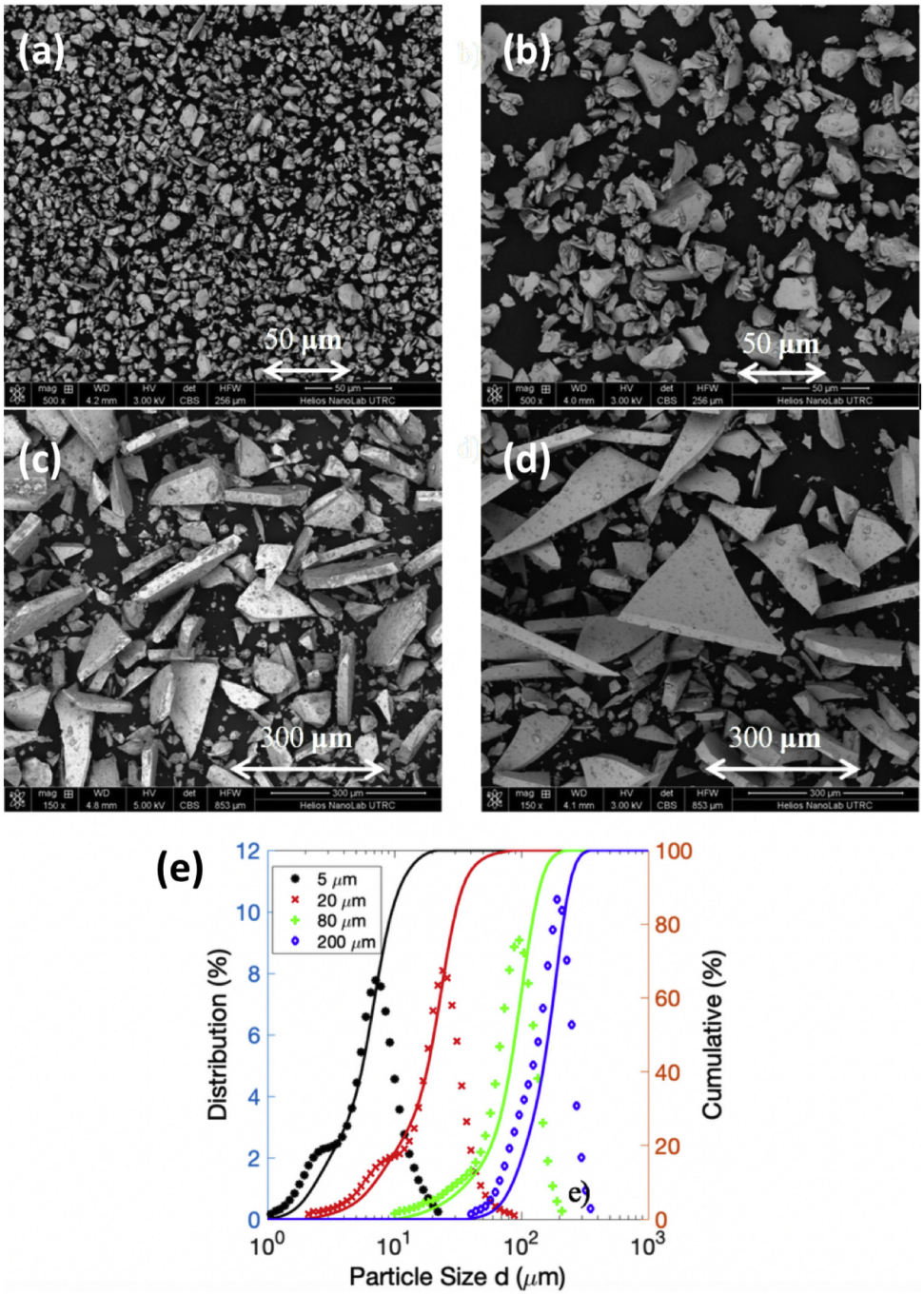

Fig. 2. (a)-(d) Scanning Electron Micrographs (SEM) of sieved melt-spun NdFeB particles having an average particle size, or equivalent spherical diameter, of 5, 20, 80, 200 µm, as determined by laser diffraction. (e) Particle size distribution of the sieved, melt-spun NdFeB particles. Solid lines are cumulative distribution.

where η_r is the relative viscosity, k is a shape-factor parameter, and ϕ_m is the maximum packing fraction. For hard spheres, k is expected to be 2.5. For non-spherical particles, k is larger than 2.5 and becomes an empirical parameter that is highly dependent on the aspect ratio and surface roughness of the particles [27].

Another widely accepted form was proposed by Krieger and Dougherty [28].

$$\eta_r = \left(1-\frac{\phi}{\phi_m}\right)^{-k\phi_m},$$

Fig. 3b shows the relative viscosity as a function of volume fraction of 20-µm particles at a fixed shear rate of 0.01 s^{-1}. The best fit values are: $k = 5$ and of $\phi_m = 0.7$ for the Mooney equation and $k = 10$ and $\phi_m = 0.69$ for the Krieger-Dougherty equation, respectively. Fitting was carried out using the least square method coded in MATLAB. For random close packing of monodisperse spheres, ϕ_m should be around 0.64. The unimodal samples have a best-fit ϕ_m value larger than 0.64, which may be explained by irreducible polydispersity with sieving. For incompressible systems, ϕ_m should never exceed one. Under this constraint, Krieger-Dougherty equation describes the experimental data better compared to the Mooney equation, which assumes an exponential form with no adjustable parameter in the exponent. The best-fit values of k and ϕ_m for unimodal and bimodal dispersions of non-spherical, melt-spun particles are included in Supporting Information Table S1. For unimodal dispersions, the k value varies from 6.3 to 15.0 while the

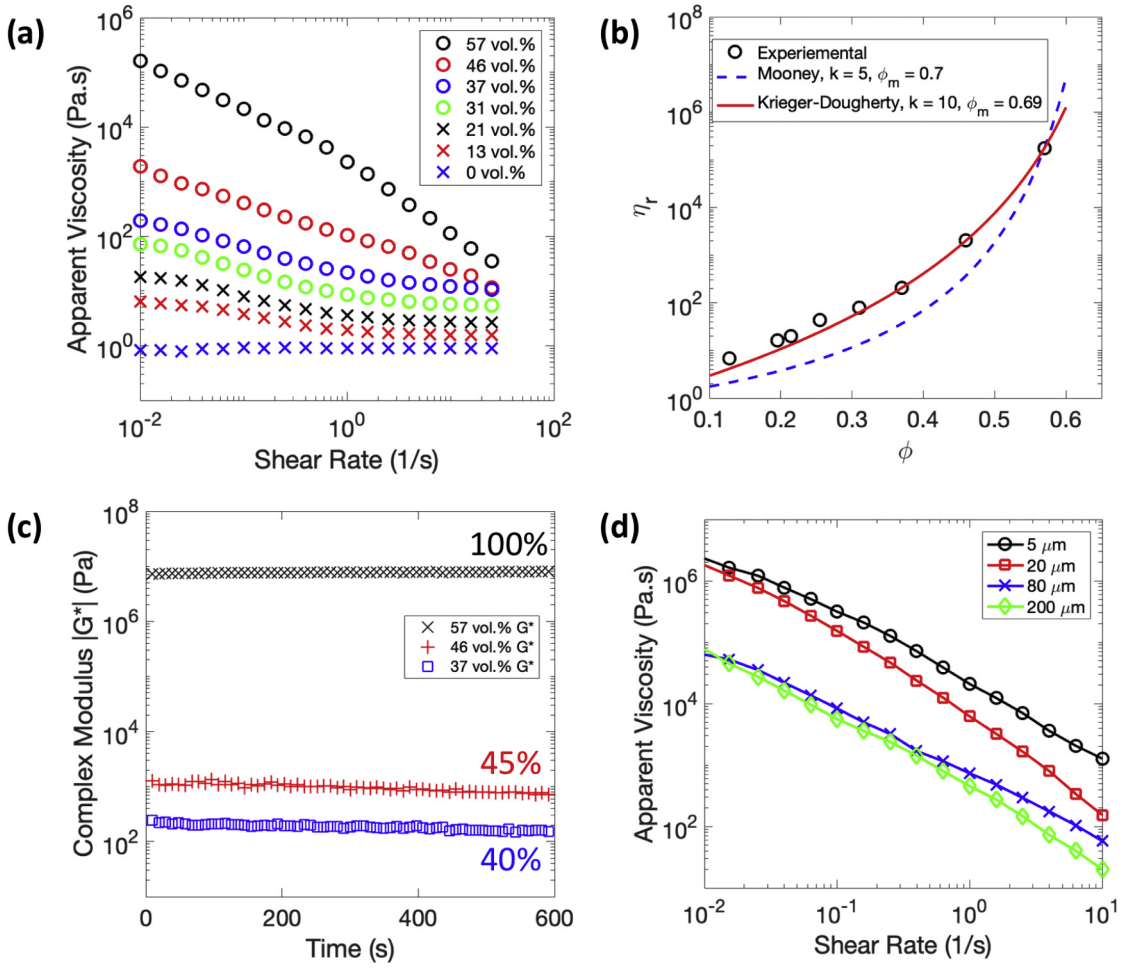

Fig. 3. (a) Flow curves of 20-μm (unimodal) NdFeB particle suspensions with different particle loadings by volume, corresponding to 0%, 50%, 65%, 75%, 80%, 85% and 90% particle loading by weight. (b) Relative viscosity (η_r) as a function of particle volume fraction (ϕ). Open symbols represent experimental viscosity data (at a shear rate of 0.01 s^{-1}). The solid and dotted lines are the best fits with the Krieger-Dougherty equation and the Mooney equation, respectively. (c) Time evolution of the complex modulus (|G*|) for 20-μm (unimodal) NdFeB particle suspensions at three different particle loadings. Strain amplitude: $\gamma_0 = 1\%$; Frequency: $\omega = 1$ rad/s; Temperature: 25 °C; Parallel plate fixture. The values shown are the ratios of |G*| measured at 600 s to that at 0 s. (d) Flow curves of suspensions containing unimodal particles of four different sizes. The particle loading is 57 vol% in all samples. Temperature: 25 °C.

ϕ_m value varies from 0.50 to 0.69. For bimodal dispersions, the k value varies from 7.0 to 11.3 while the ϕ_m value varies from 0.64 to 0.75. Determining the exact relationship between these model parameters and particle attributes such as size distribution, aspect ratio, and roughness is beyond the scope of this study. Although these values were obtained empirically from data fitting, the bimodal dispersions tend to have a higher ϕ_m value which is consistent with the Farris effect explored in the next section.

To assess the stability, or more specifically, the sedimentation propensity of the suspensions, the magnitude of complex modulus, or |G*|, of the suspensions was measured as a function of time as small amplitude oscillatory shear ($\gamma_0 = 1\%$; $\omega = 1$ rad/s) was applied to the sample confined between two parallel plates. Fig. 3c shows the time sweep results for three different particle loadings (37%, 46%, and 57%, by volume). The ratios of |G*| measured at 600 s to the initial value (i.e., $|G^*|_{600\ s}/|G^*|_{0\ s}$) are included in the plot for reference. For the 37% and 46% samples, the complex modulus decreases over time. The decrease is attributed to the sedimentation of particles due to the large density difference between the particles and the binder, resulting in a lower effective concentration near the upper parallel plate at which the torque is measured. In the case of the 57% sample, it is hypothesized that the high loading of particles hinders particle motions as the particle will have to get pass each other before sedimentation occurs. As a result, the complex modulus remains fairly constant over time, which is desirable for consistent printing.

The effect of average particle size on the steady shear rheology is shown in Fig. 3d. The particle loading of all four samples is kept at 57 vol%. The two samples containing smaller particles (5 μm and 20 μm) clearly showed a higher apparent viscosity compared to the samples containing larger plate-like samples (80 μm and 200 μm). The difference between these samples is attributed to the different levels of particle-particle interactions and possibly particle orientation (in the case of plate-like samples). First, for the same volume fraction, the number density of smaller particles will be higher than that of the larger particles. This results in a larger contribution of particle-particle interactions to the overall viscosity [13]. Second, in the case of the larger plate-like particles having a high aspect ratio, they may become aligned as the loading increases due to excluded volume interactions, which are well documented in the liquid crystalline literature [29,30]. Third, these particles may become aligned along the shear plane because of the hydrodynamic forces associated with the squeeze flow during sample loading and shear flow during experiments. The shear stress contribution of particles towards the overall suspension viscosity decreases as the degree of shear-plane alignment increases [31]. The alignment of plate-like particles has been observed and reported by Paranthaman et al. for magnets 3D printed using the BAAM method. Scanning electron microscopy (SEM) was performed on the printed magnets in this study; however, no clear preferentially alignment of the particles was observed. A representative SEM image is included in Supporting Information.

3.3. Using particle polydispersity to increase the highest printable particle loading

For a given feed pressure of 100 psi, the highest printable particle loading was determined to be 55% by volume for the 20-μm particle sample. In this section, we explore the idea of introducing particle polydispersity to increase the maximum packing fraction. This idea is inspired by the seminal paper by Farris [32], who studied the effects of mixing two different sizes of spherical particles. Physically, the smaller particles of an appropriate size ratio to the larger ones will fill the interstices between the large particles, thereby maximizing the total solid volume fraction [33]. Most of the existing studies, including the original work, focus on spherical particles. In this study, we define the size ratio of the irregular non-spherical particles as the ratio between the larger particle size (a_l) and the smaller particle size (a_s), using the equivalent spherical particle diameter as the characteristic particle size.

$$\delta = a_l/a_s$$

Additionally, we use the volume fraction of the larger particles (ζ) relative to the total volume fraction to describe the samples prepared by mixing any two different sizes:

$$\zeta = \phi_l/\phi$$

where ϕ_l is the volume fraction occupied by the large particles and ϕ is the total volume fraction occupied by particles, both large and small.

Fig. 4a shows the effects of particle size ratio (δ) as a function of the volume fraction of large particles (ζ) for a given shear rate of 0.01 s^{-1}. The relative viscosity first decreases and then increases as a function of increasing ζ. Similar trends have been reported by a number of authors. For instance, Dames and Fiske reported a ζ-value of around 0.3 to attain the minimal viscosity [34,35], whereas Shapiro et al. reported the minimum occurs at $\zeta > 0.5$ [36]. As shown in Fig. 4a, the minimum viscosity occurred at $\zeta = 0.67$, consistent with numerical simulation results obtained by Morris and colleagues who suggested the lowest viscosity occurred for $0.5 < \zeta < 0.7$ [17]. However, Morris *et al.* considered bimodal mixing of spherical particles instead of non-spherical particles and the simulated particle size ratio varies within a much narrower range (from 2 to 4). In terms of size ratio (δ), the minimal viscosity was observed for $\delta = 16$, which is consistent with the experimental values reported by Brouwers et al. and Dames et al. [37] for highly concentrated bimodal suspensions. Fig. 4b summarizes the relative viscosity data as a function of total particle loading (at a fixed ζ-value of 0.67). For the same relative viscosity value, a δ-value of 16 yields the highest particle loading. For $\delta = 16$ and $\zeta = 0.67$, dispersions with a total particle loading of as high as 65 vol% was successfully prepared. Muller et al. [38] reported an experimentally achievable particle concentration of 57.5 vol% for polyacrylic glitters with a similar shape.

3.4. Density and surface finish of UADW magnets

One drawback of Fused Deposition Modeling (FDM) and Big Area Additive Manufacturing (BAAM) printed magnets is their high porosity because of the elliptical-shaped cross-sections of the infills and rapid solidification of polymer melts. Measured density of FDM and BAAM magnets can be 10 to 20% lower than the theoretical density calculated from the nominal composition of the feedstock [5]. Extrusion-based DW uses ink formulations with viscosities orders of magnitude lower than FDM and BAAM. Surface tension can therefore facilitate the fusion between deposited inks, minimizing or removing any voids. Since polydispersity lowers the ink viscosity, the void fraction could be further reduced. Experimentally, for 55 vol% of 20-μm unimodal particles, the density of the printed magnets was measured to be 4.4 g/cm^3, which closely matches the expected theoretical density of 4.4 g/cm^3 (assuming a linear combination of input material densities and no voids). As the nominal volume fraction was further increased to 60%, the average density of the magnets printed from unimodal particles increased to 4.6 g/cm^3 (based on three samples), which is 8% lower than the expected theoretical density of 5.0 g/cm^3. The difference is attributed to the increasing difficulty in dispersing the particles uniformly as the particle loading and viscosity approach the theoretical limit. For the bimodal mixing of 5-μm and 80-μm particles at $\zeta = 0.67$ and $\phi = 0.65$, the resulting printed magnet sample has a density of 5.0 g/cm^3, matching the theoretical density. The highest particle loading was found to be ca. 65 vol% for an optimized δ-value of 16 and ζ-value of 0.67, limited by the abundance of binder and/or mixing method. A higher loading than these values resulted in an inhomogeneous sample with clearly visible spherical clusters (see Supporting Information).

Although bimodal mixing increased the maximum printable volume fraction, the presence of larger particles in bimodal print mixture also resulted in shape distortion and a rougher surface, compromising the quality of the surface finish. Fig. 5a and c show the top and side views of a magnet printed from unimodal 20-μm non-spherical particles,

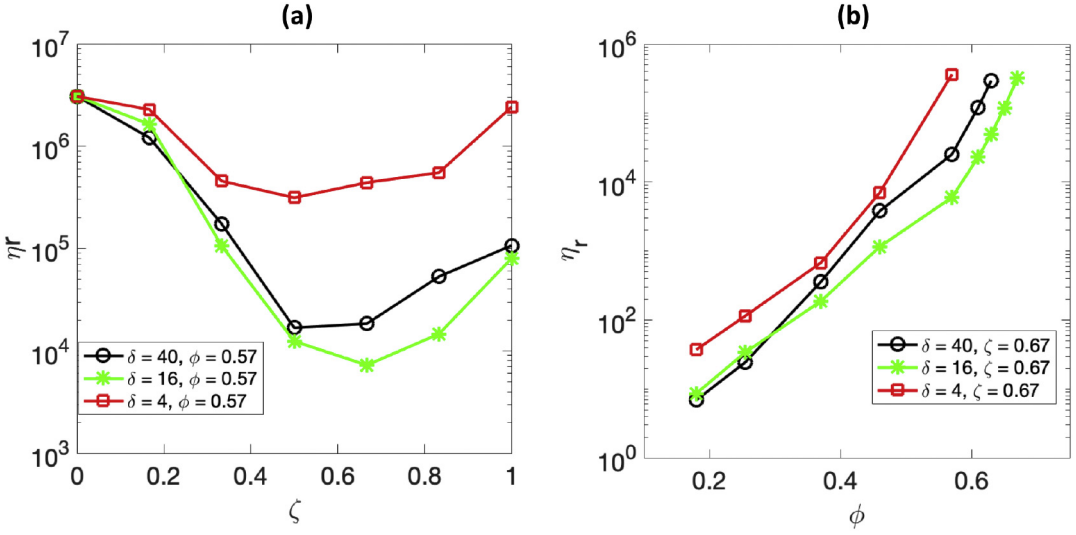

Fig. 4. (a) Relative viscosity (η_r) as a function of the volume fraction of the large particles (ζ) for different particle size ratios (δ). Samples with $\delta = 4$, 16, and 40 were prepared by mixing 5-μm particles with 20-μm, 80-μm, and 200-μm particles, respectively. Shear rate: 0.01 s^{-1}. Temperature: 25 °C. (b) Relative viscosity (η_r) as a function of the total particle fraction (ϕ) at a fixed ζ of 0.67 for different particle size ratios (δ). Shear rate: 0.01 s^{-1}. Temperature: 25 °C.

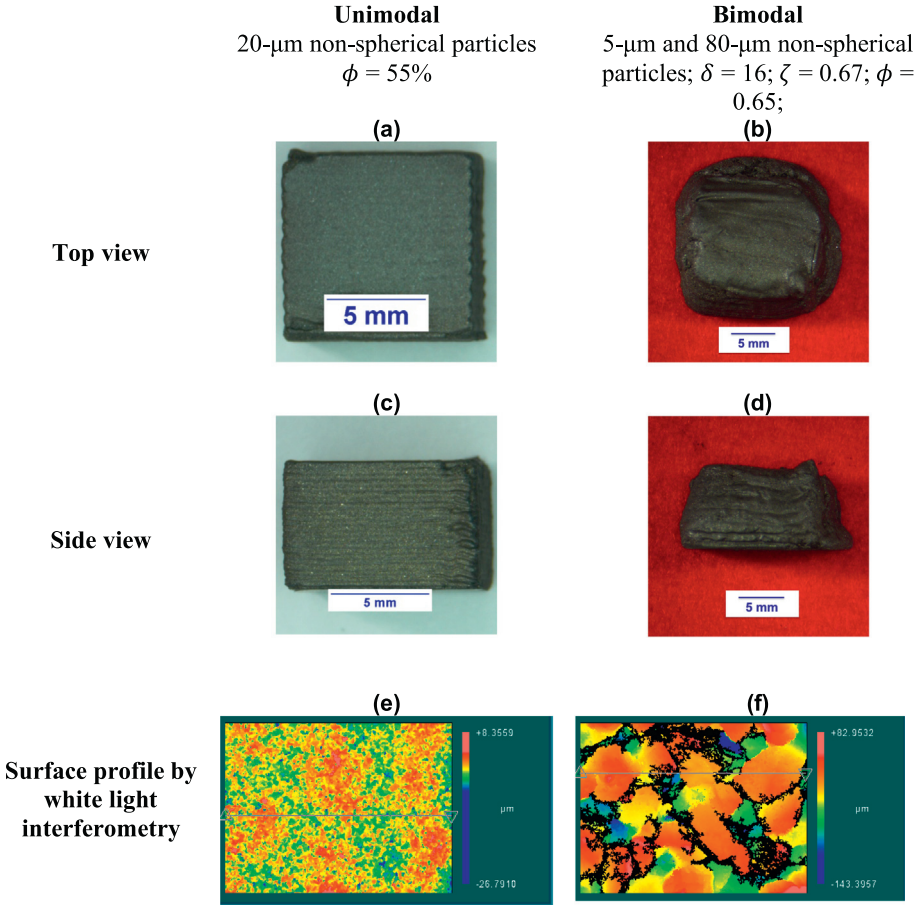

Fig. 5. Top view (a, b) and side view (c, d) of magnets printed from unimodal and bimodal suspensions. In the bimodal case, a larger nozzle tip of 1.6 mm and a layer thickness of 800 μm were used to accommodate for the larger particles present, whereas a 400-μm (dia.) tip and a layer thickness of 200 μm were used for the unimodal case. In both cases, the surface profile was captured using white light interferometry with a scanned area of 0.7 mm × 0.5 mm on the top surface. The color bar shows the height variation following the horizontal lines drawn across the sample.

compared to that of a magnet printed from a bimodal mixture of 5-μm and 80-μm non-spherical particles with maximum loading (Fig. 5b and d). The use of larger particles requires a larger nozzle, which increases the layer thickness and consequently exacerbate the "staircase effect". Fig. 5e and f show in greater detail the corresponding (top) surface profile of these samples measured using white light interferometry. For a scanned area of 0.7 mm × 0.5 mm, the unimodal sample has an arithmetic mean roughness (R_a) of 1.393 μm and a ten-point height (R_z) of 28.14 μm, whereas the bimodal sample has a R_a-value of 12.971 μm and a R_z-value of 188.24 μm. The roughness of the bimodal sample is an order of magnitude higher compared to the unimodal sample.

3.5. Magnetic performance of UADW magnets

Fig. 6a and b show the second quadrant demagnetization loop and energy product of post-cured magnets prepared using unimodal spherical and unimodal non-spherical particles. Remanence, intrinsic coercivity, and energy product are key attributes of a magnet. Remanence (B_r) refers to the magnetization remained in a ferromagnetic material after an external magnetic field is removed and is the y-intercept in the second quadrant plots. Intrinsic coercivity (H_{ci}) is the strength of the magnetic field required to reduce the magnetic polarization to zero and corresponds to the x-intercept. Energy product, $(BH)_{max}$, represents the magnetostatic energy a permanent magnet material can store, and is therefore a direct indicator of magnetic strength. The higher the B_r, H_c, and $(BH)_{max}$ values, the stronger the magnet. Table 1 summarizes the magnetic performance of some of the magnets tested in this study.

In the case of unimodal mixing, the highest printable loading for the non-spherical plate-like particles is 55 vol%, which is lower than that for unimodal spherical particles (60 vol%). The highest loading is mainly limited by the working viscosity, and non-spherical particle suspensions tend to have a higher viscosity because of the increased particle-particle interactions through hydrodynamics and/or direct particle contacts [39]. As shown in Table 1, the magnets printed from spherical and non-spherical particles showed similar H_{ci} values (9.50 kOe vs. 9.42 kOe) at the corresponding highest loading of 60 vol% and 55 vol%, respectively. For a given type of feedstock particles, the higher solid loading, the higher the remanence (B_r), as reported in our previous study for the spherical particles [1]. Although the spherical particle samples have a higher particle loading of 60 vol%, the non-spherical samples at 55 vol% showed considerably higher B_r and $(BH)_{max}$ values (4.66 kG and 4.72 MGOe), compared to the spherical samples with B_r = 3.76 kG and $(BH)_{max}$ = 3.05 MGOe. Such difference may be explained by a higher B_r (9.03 kG) of the non-spherical melt-spun particles relative to the spherical particles produced from atomization (7.30 kG). If the measured remanence of the printed magnets is normalized by the corresponding powder B_r, the spherical and non-spherical samples possess similar "relative remanence" values (51.5% vs. 51.6% of the feedstock powder B_r).

To further increase the particle loading of non-spherical particles and consequently the remanence and energy product, bimodal mixing is used. A loading as high as 65 vol% was achieved by mixing 80-μm and 5-μm particles (δ = 16; ζ = 0.67). The magnets printed from this suspension has a similar H_{ci}, but has a B_r value of 5.88 kG and a $(BH)_{max}$ value of 7.26 MGOe, which are 26% higher and 54% higher compared

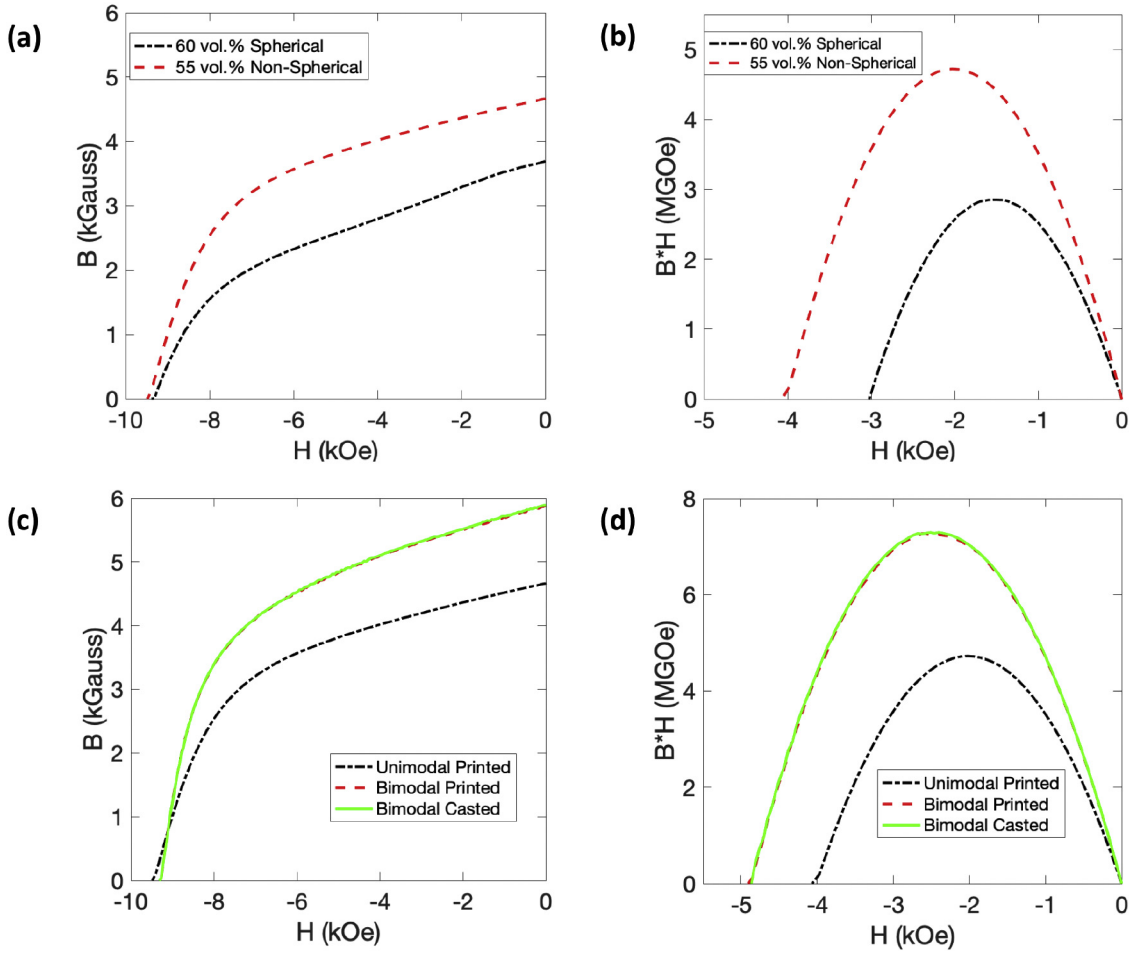

Fig. 6. (a-b) Second quadrant hysteresis curve and energy product of highest printable loading of unimodal spherical and unimodal non-spherical particles at 60 vol% and 55 vol%, respectively. Particle size: 20 μm. The magnetic performance of spherical particles for comparison was acquired from author's previous work [1]. (c-d) Second quadrant hysteresis curve and energy product of "unimodal printed", "bimodal printed", and "bimodal casted" magnets. The unimodal sample contained 20-μm melt-spun particles at 55 vol%, and the bimodal sample was prepared by mixing 80-μm and 5-μm particles with $\zeta = 0.67$. The total particle loading in the "bimodal printed" and "bimodal casted" magnets is 65 vol%.

to the unimodal case. Using bimodal mixing to compensate for the associated increase in viscosity for non-spherical particles, the magnetic performance, namely, the remanence and energy product, was further improved. Additionally, the properties of UADW magnets with bimodal mixing rival those of a casted magnet ($B_r = 5.89$ kG; $H_c = 9.3$ kOe; $BH_{max} = 7.31$ MGOe). UADW is much more versatile than casting when it comes to printing magnets of more complex shapes without using a mold for casting and printing directly onto existing components for seamless integration. This point is illustrated in Fig. 7a, which shows a mechanical test coupon and a magnet sensor printed onto a glass slide.

Fig. 7b summarizes and compares the magnetic performance of polymer-bonded magnets prepared by various 3D printing methods and injection molding (IM). In addition to UADW, magnets have also been 3D printed using Big Area Additive Manufacturing (BAAM), Selective Laser Sintering (SLS), Binder Jetting, and Thermo-curing Direct Write (DW). The feedstock powder and the associated intrinsic magnetic properties vary in each study, so "relative remanence" and "relative intrinsic coercivity" are calculated by normalizing the measured B_r and H_{ci} of the magnets with the corresponding B_r and H_{ci} of the feedstock powder. UADW combined with bimodal mixing (labeled as "bimodal-UADW" in the figure) offers the highest relative remanence and relative intrinsic coercivity. The high remanence may be explained by the increase in the overall particle loading with minimal porosity.

Compared to methods such as BAAM and FDM, the relatively low processing viscosity of UADW prior to UV curing allows the fusion between extrudates, thereby minimizing the void within the printed magnets. For methods like SLS and binder-jetting, the porosity of parts depends largely on: (i) how the powder layer is discharged and spread onto the build plate [9] and (ii) the ink infiltration for binder-jetting and the sintering process for SLS. In terms of relative intrinsic coercivity, magnets produced from the UADW method have a value close to one, suggesting the successful preservation of intrinsic powder properties

Table 1
Comparison of bulk density, highest printable particle loading, and the resulting properties of magnets prepared by different fabrication methods (UADW vs. casting), mixing strategies (unimodal vs. bimodal), and types of feedstock particles (spherical vs. non-spherical). Sph.: spherical atomized particles; N-Sph.: non-spherical melt-spun particles.

Conditions	Mixing/geometry	ρ (g/cc)	Highest printable loading (by volume)	B_r (kG)	H_{ci} (kOe)	$(BH)_{max}$ (MGOe)
UADW	Unimodal/ Sph.	4.0	60%	3.76	9.50	3.05
UADW	Unimodal/ N-Sph.	4.4	55%	4.66	9.42	4.72
UADW	Bimodal / N-Sph.	5.2	65%	5.88	9.39	7.26
Casted	Bimodal / N-Sph.	5.3	65%	5.89	9.30	7.31

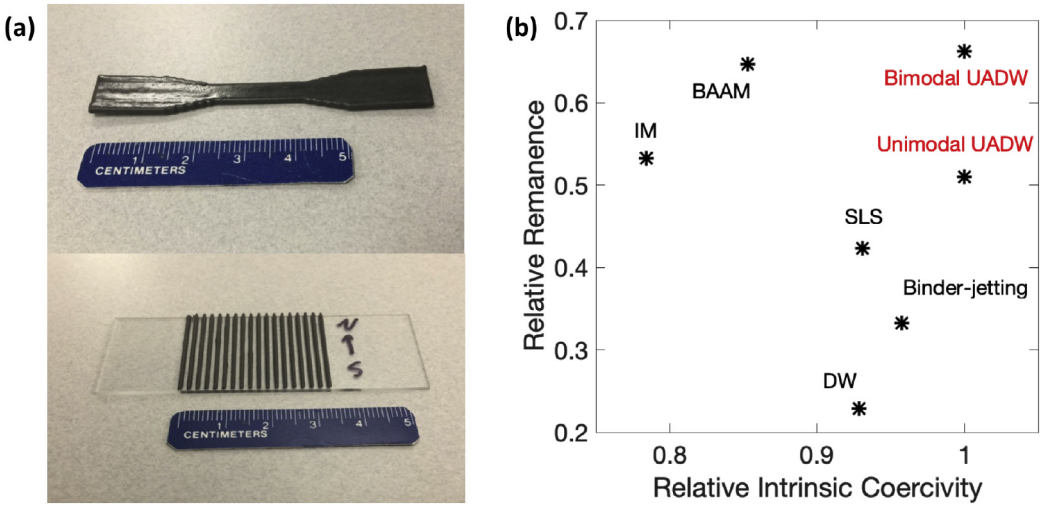

Fig. 7. (a) Printed dumbbell shape coupon and magnetic sensors on glass substrate. These samples were printed using 46 vol% unimodal 20-μm melt-spun particles. (b) Comparison of performance for magnets prepared by different methods, namely, Unimodal-UADW and Bimodal-UADW (this work), Injection Molding (IM), Big Area Additive Manufacturing (BAAM), Selective Laser Sintering (SLS), Binder-jetting, and Direct Write (DW). The higher the remanence value and the higher the intrinsic coercivity value, the better the magnet performance. The figure is an update of author's previous work with unimodal UV-Assisted Direct Write (UADW) data [1]. Reprinted with permission from Elsevier.

during the processing. The difference in relative intrinsic coercivity between different methods is mainly caused by the difference in processing temperature. Methods like IM and BAAM requires melting of the polymer carrier at a temperature typically higher than 200 °C, which may disturb the alignment of the spins and cause particle oxidation. The UADW process was carried out at room temperature, followed by post-curing at 60 °C to minimize degradation associated with the heat treatment. Combining the bimodal mixing method with UADW enables the fabrication of magnets with the best magnetic performance reported to-date.

4. Conclusions and outlook

This paper builds on a recently developed 3D printing method called UV-assisted Direct Write (UADW) to fabricate magnets from highly concentrated plate-like magnetic particles. Compared to spherical particles reported in a previous study [1], the plate-like particles prepared from melt spinning are magnetically stronger — having a higher remanence (B_r) and higher energy product $(BH)_{\max}$. However, suspensions containing the plate-like particles tend to have much higher viscosities, which further limit the maximum particle loading in the feedstock suspensions for UADW. To overcome this limitation, two different sizes of plate-like particles were mixed to increase the polydispersity and thus lower the overall viscosity, taking advantage of the well-known "Farris effect" in rheology [40]. Intuitively, Farris effect may be understood in terms of the filling of smaller particles in the interstitial space between the larger particles. Using an appropriate size ratio ($\delta = 16$) and volume ratio ($\zeta = 0.67$) between the "large" particles and "small" particles, a suspension containing 65 vol% total particle loading was prepared and used for 3D printing with UADW. The resulting magnets have an intrinsic coercivity (H_{ci}) of 9.30 kOe, a remanence (B_r) of 5.88 kG, and an energy product ($(BH)_{max}$) of 7.26 MGOe. These values are by far the highest in the literature of 3D printed magnets and rival those of casted polymer-bonded magnets. Unlike casting, 3D printing is much more versatile in producing functional components with different form factors. The mechanical and magnetic properties may further be engineered through shape and topology optimization. Scientifically, the rheological data presented in this study provides the basis for understanding and modeling highly concentrated suspensions of non-spherical particles, which remains largely unexplored. Technologically, the magnetic performance of 3D printed magnets may be further improved through material formulations and process control. Of particular interest is to explore the use of anisotropic magnetic particles and how to control their alignment through in-situ processing [41] or post-processing [42], which may lead to even stronger magnets as suggested by other authors. All in all, this paper describes rheology-enabled 3D printing of polymer-bonded magnets with the best magnetic performance reported in the literature thus far.

Credit author statement

S. Dardona and A. Ma are responsible for conceptualization, funding acquisition, and project administration. A. Shen, X. Peng, and C. P. Bailey are responsible for data curation and analysis. A. Shen and A. Ma are responsible for writing the original manuscript draft. All authors contributed to reviewing and editing the manuscript before submission.

Acknowledgement

The authors acknowledge financial support from United Technologies Research Center (UTRC) and Chenyu Wang's assistance with MATLAB optimization programming. We also thank Anton Paar USA Inc. for providing an instrument and offering A. Shen an Anton Paar Research Fellowship. We would like to thank Greg Umana of Magnetic Instrumentation for providing magnetization services and technical guidance and Jim Herchenroeder of Magnequench for his advice on the properties of NdFeB powders.

Competing interests

This work has been funded by United Technologies Research Center and Anton Paar USA Inc. The authors declare no further potential conflict of interest.

Appendix A. Supplementary data

Supplementary data to this article can be found online at https://doi.org/10.1016/j.matdes.2019.108133.

References

[1] A. Shen, C.P. Bailey, A.W.K. Ma, S. Dardona, UV-assisted direct write of polymer-bonded magnets, J. Magn. Magn. Mater. 462 (2018) 220–225, https://doi.org/10.1016/j.jmmm.2018.03.073.

[2] D. Kokkinis, M. Schaffner, A.R. Studart, Multimaterial magnetically assisted 3D printing of composite materials, Nat. Commun. 6 (2015)https://doi.org/10.1038/ncomms9643.

[3] Y. Matsuura, Recent development of Nd-Fe-B sintered magnets and their applications, J. Magn. Magn. Mater. 303 (2 SPEC. ISS) (2006) 344–347, https://doi.org/10.1016/j.jmmm.2006.01.171.

[4] B.M. Ma, J.W. Herchenroeder, B. Smith, M. Suda, D. Brown, Z. Chen, Recent development in bonded NdFeB magnets, J. Magn. Magn. Mater. 239 (1–3) (2002) 418–423, https://doi.org/10.1016/S0304-8853(01)00609-6.

[5] L. Li, A. Tirado, I.C. Nlebedim, O. Rios, B. Post, Kunc, R.R. Lowden, E. Lara-Curzio, R. Fredette, J. Ormerod, T.A. Lograsso, M.P. Paranthaman, Big Area Additive Manufacturing of high performance bonded NdFeB magnets, Sci. Rep. 6 (1) (2016) 36212, https://doi.org/10.1038/srep36212.

[6] C. Huber, C. Abert, F. Bruckner, M. Groenefeld, S. Schuschnigg, I. Teliban, C. Vogler, G. Wautischer, R. Windl, D. Suess, 3D printing of polymer-bonded rare-earth magnets with a variable magnetic compound fraction for a predefined stray field, Sci. Rep. 7 (1) (2017) 1–8, https://doi.org/10.1038/s41598-017-09864-0.

[7] T. Habijan, C. Haberland, H. Meier, J. Frenzel, J. Wittsiepe, C. Wuwer, C. Greulich, T.A. Schildhauer, M. Köller, (2013). The biocompatibility of dense and porous nickel-titanium produced by selective laser melting, Material Science Engineering C 33 (1) (2013) 419–426, https://doi.org/10.1016/j.msec.2012.09.008.

[8] H. Shokrollahi, A review of the magnetic properties, synthesis methods and applications of maghemite, J. Magn. Magn. Mater. 426 (2017) 74, https://doi.org/10.1016/j.jmmm.2016.11.033.

[9] M.P. Paranthaman, C.S. Shafer, A.M. Elliott, D.H. Siddel, M.A. McGuire, R.M. Springfield, J. Ormerod, Binder Jetting: a novel NdFeB bonded magnet fabrication process, JOM 68 (7) (2016) 1978–1982, https://doi.org/10.1007/s11837-016-1883-4.

[10] B.G. Compton, J.W. Kemp, T.V. Novikov, R.C. Pack, C.I. Nlebedim, C.E. Duty, O. Rios, M.P. Paranthaman, Direct-write 3D printing of NdFeB bonded magnets, Mater. Manuf. Process. 0 (0) (2016) 1–5, https://doi.org/10.1080/10426914.2016.1221097.

[11] L. Li, B. Post, V. Kunc, A.M. Elliott, M.P. Paranthaman, Additive manufacturing of near-net-shape bonded magnets: prospects and challenges, Scr. Mater. 135 (2016) 100–104, https://doi.org/10.1016/j.scriptamat.2016.12.035.

[12] A. McFarlane, K. Bremmell, J. Addai-Mensah, Improved dewatering behavior of clay minerals dispersions via interfacial chemistry and particle interactions optimization, J. Colloid Interface Sci. 293 (1) (2006) 116–127, https://doi.org/10.1016/j.jcis.2005.06.034.

[13] A. Otsuki, G. Bryant, Characterization of the interactions within fine particle mixtures in highly concentrated suspensions for advanced particle processing, Adv. Colloid Interf. Sci. 226 (2015) 37–43, https://doi.org/10.1016/j.cis.2015.07.005.

[14] A.V. Zhukov, Crystal microstructure and rheology of highly-concentrated ferromagnetic suspensions, Fluid Dynamics 41 (5) (2006) 784–794, https://doi.org/10.1007/s10697-006-0095-y.

[15] Magnequench Datasheet2017.

[16] R.G. Larson, The Structure and Rheology of Complex Fluids, Oxford University Press, 1999.

[17] S. Pednekar, J. Chun, J.F. Morris, Bidisperse and polydisperse suspension rheology at large solid fraction, J. Rheol. 62 (2) (2018) 513–526, https://doi.org/10.1122/1.5011353.

[18] S.L. Morissette, J.A. Lewis, P.G. Clem, J. Cesarano, D.B. Dimos, Direct-write fabrication of Pb(Nb,Zr,Ti)O_3 devices: influence of paste rheology on print morphology and component properties, J. Am. Ceram. Soc. 84 (11) (2001) 2462–2468, https://doi.org/10.1111/j.1151-2916.2001.tb01036.x.

[19] A. Shen, D. Caldwell, A.W.K. Ma, S. Dardona, Direct write fabrication of high-density parallel silver interconnects, Additive Manufacturing 22 (2018) 343–350, https://doi.org/10.1016/j.addma.2018.05.010.

[20] S. Dardona, A. Shen, C. Tokgoz, Direct write fabrication of a wear sensor, IEEE Sensors J. 18 (8) (2018) 3461–3466, https://doi.org/10.1109/JSEN.2018.2810839.

[21] Z. Zguris, Formlabs White Paper, 2016.

[22] C.W. Macosko, Rheology: Principles, Measurements and Applications, Wiley, 1994.

[23] C. Tuitz, U. Exner, A. Preh, B. Grasemann, The influence of particle orientation on the loading condition of pebbles in fluvial gravel, Granul. Matter 14 (5) (2012) 639–649, https://doi.org/10.1007/s10035-012-0365-9.

[24] A.W.K. Ma, F. Chinesta, M.R. Mackley, The rheology and modeling of chemically treated carbon nanotubes suspensions, J. Rheol. 53 (3) (2009) 547–573, https://doi.org/10.1122/1.3093105.

[25] W.K.A. Ma, F. Chinesta, A. Ammar, M.R. Mackley, Rheological modeling of carbon nanotube aggregate suspensions, J. Rheol. 52 (6) (2008) 1311–1330, https://doi.org/10.1122/1.2982932.

[26] M. Mooney, The viscosity of a concentrated suspension of spherical particles, J. Colloid Sci. 6 (1951) 162–170, https://doi.org/10.1016/0095-8522(51)90036-0.

[27] C. Tanford, Physical Chemistry of Macromolecules, Wiley, 1961.

[28] I.M. Krieger, T.J. Dougherty, A mechanism for non-Newtonian flow in suspensions of rigid spheres, Transactions of the Society of Rheology 3 (1959) 137–152, https://doi.org/10.1122/1.548848.

[29] L. Onsager, The effects of shape on the interaction of colloidal particles, Ann. N. Y. Acad. Sci. 51 (4) (1949) 627–659, https://doi.org/10.1111/j.1749-6632.1949.tb27296.x.

[30] A.M. Donald, A.H. Windle, S. Hanna, Liquid Crystalline Polymers, Cambridge University Press, 2006.

[31] E.J. Hinch, L.G. Leal, Rotation of small non-axisymmetric particles in a simple shear flow, J. Fluid Mech. 92 (1979) 591–608, https://doi.org/10.1017/S002211207900077X.

[32] R.J. Farris, Prediction of the viscosity of multimodal suspension from unimodal viscosity data, Transactions of the Society of Rheology 12 (1968) 281–301, https://doi.org/10.1122/1.549109.

[33] M.M. Rueda, M.C. Auscher, R. Fulchiron, T. Périé, G. Martin, P. Sonntag, P. Cassagnau, Rheology and applications of highly filled polymers: a review of current understanding, Prog. Polym. Sci. 66 (2017) 22–53, https://doi.org/10.1016/j.progpolymsci.2016.12.007.

[34] T.J. Fiske, S.B. Railkar, D.M. Kalyon, Effects of segregation on the packing of spherical and nonspherical particles, Powder Technol. 81 (1994) 57–64, https://doi.org/10.1016/0032-5910(94)02862-1.

[35] J.S. Chong, E.B. Christiansen, A.D. Baer, Rheology of concentrated suspensions, J. Appl. Polym. Sci. 15 (1971) 2007–2021, https://doi.org/10.1002/app.1971.070150818.

[36] A.P. Shapiro, R.F. Probstein, Random packings of spheres and fluidity limits of monodisperse and bidisperse suspensions, Phys. Rev. Lett. 68 (1992) 1422–1425, https://doi.org/10.1103/PhysRevLett.68.1422.

[37] B. Dames, B.R. Morrison, N. Willenbacher, An empirical model predicting the viscosity of highly concentrated, bimodal disperions with colloidal interactions, Rheol. Acta 40 (5) (2001) 434–440, https://doi.org/10.1007/s003970100171.

[38] S. Mueller, E.W. Llewellin, H.M. Mader, The rheology of suspensions of solid particles, Proceedings of The Royal Society A 466 (2010) 1201–1228, https://doi.org/10.1098/rspa.2009.0445.

[39] A. Otsuki, G. Bryant, Characterization of the interactions within fine particle mixtures in highly concentrated suspensions for advanced particle processing, Adv. Colloid Interf. Sci. 226 (2015) 37–43, https://doi.org/10.1016/j.cis.2015.07.005.

[40] N.K.O. Ojijo, E. Shimoni, Minimization of cassava paste flow properties using the “Farris effect”, LWT Food Sci. Technol. 41 (1) (2008) 51–57, https://doi.org/10.1016/j.lwt.2007.01.020.

[41] Y. Kim, H. Yuk, R. Zhao, S.A. Chester, X. Zhao, Printing ferromagnetic domains for untethered fast-transforming soft materials, Nature Letter 558 (2018) 274–279, https://doi.org/10.1038/s41586-018-0185-0.

[42] K. Gandha, L. Li, I.C. Nlebedim, B.K. Post, V. Kunc, B.C. Sales, J. Bell, M.P. Paranthaman, Additive manufacturing of anisotropic hybrid NdFeB-SmFeN nylon composite bonded magnets, J. Magn. Magn. Mater. 467 (June) (2018) 8–13, https://doi.org/10.1016/j.jmmm.2018.07.021.